

Spin to charge conversion in Si/Cu/ferromagnet systems investigated by ac inductive measurements

Ei Shigematsu,¹ Lukas Liensberger,^{2,3} Mathias Weiler^{Ⓞ,2,3,*} Ryo Ohshima^{Ⓞ,1} Yuichiro Ando,¹ Teruya Shinjo,¹ Hans Huebl^{Ⓞ,2,3,4} and Masashi Shiraishi^{1,†}

¹*Department of Electronics Science and Engineering, Kyoto University, 615–8510 Kyoto, Japan*

²*Walther-Meißner-Institut, Bayerische Akademie der Wissenschaften, 85748 Garching, Germany*

³*Physik-Department, Technische Universität München, 85748 Garching, Germany*

⁴*Munich Center for Quantum Science and Technology (MCQST), 80799 München, Germany*

 (Received 17 June 2020; revised 7 December 2020; accepted 2 March 2021; published 19 March 2021)

Semiconductor/ferromagnet hybrid systems are attractive platforms for investigation of spin conversion physics, such as the (inverse) spin Hall effect. However, the superimposed rectification currents originating from anisotropic magnetoresistance have been a serious problem preventing unambiguous detection of dc spin Hall electric signals in semiconductors. In this study, we applied a microwave frequency inductive technique immune to such rectification effects to investigate the spin to charge conversion in heterostructures based on Si, one of the primitive semiconductors. The Si doping dependence of the spin-orbit torque conductivity was obtained for the Si/Cu/NiFe trilayer system. A monotonous modulation of the spin-orbit torque conductivity by doping and relative sign change of spin to charge conversion between the degenerate *n*- and *p*-type Si samples were observed. These results unveil spin to charge conversion mechanisms in semiconductor/metal heterostructures and show a pathway for further exploration of spin-conversion physics in metal/semiconductor heterostructures.

DOI: [10.1103/PhysRevB.103.094430](https://doi.org/10.1103/PhysRevB.103.094430)

I. INTRODUCTION

Spin to charge conversion [1–3] has been one of the central research topics in spintronics, evoking both scientific interest and expectation for industrial applications. This phenomenon enables an observation of spin current as an electromotive force by using the spin-orbit interaction (SOI) and spin-dependent momentum scattering, even though spin current is not a conservative quantity and one cannot measure it directly. Therefore, spin to charge conversion has been regarded as an important research target in the field of spintronics, and its efficiency factors, i.e., spin Hall conductivity, spin Hall angle, and Rashba-Edelstein length, have been identified as crucial indices in spintronic materials. Most reports on spin to charge conversion are limited to metallic materials, some of which exhibit high conversion efficiency due to their large SOI [4]. Besides investigations of primitive spin conversion characteristics, control over the spin to charge conversion properties is also an intriguing research issue. In this viewpoint, semiconductors are a promising research field, which unites flourishing spintronic physics with conventional semiconductor physics since carrier concentration in semiconductors can be modulated by doping and gating. For example, strong SOI in heavily doped semiconductor silicon [5] and modulation of the inverse spin Hall effect in GaAs [6] were demonstrated.

A typical experimental implementation of spin to charge conversion consists of (i) injection of spin current from a ferromagnetic material and (ii) spin to charge conversion in an adjacent material. To realize this scheme, spin pumping in detector material/ferromagnet bilayer systems is widely employed, where the detector material is spin Hall active. Various nonmagnetic [2,7,8] or ferromagnetic materials [9–11] can be used as a spin detector. Spin pumping is the phenomenon which induces spin current flow driven by exciting ferromagnet resonance (FMR) in the magnetically ordered layer [2,12–14]. Most reports on spin-pumping experiments employed dc detection of spin to charge conversion electromotive forces with in-plane magnetization of the ferromagnet. This experimental scheme has been the basis for many reports on spintronic properties of various materials such as nonmagnetic metals [2,7,8], semimetals [15,16], semiconductors [5,6], and topological insulators [17]. However, an influence of the rectification effects in the ferromagnetic metal [18–21] hinders precise evaluation of spin to charge-conversion-related dc signals. Additionally, in some combinations of nonmagnetic and ferromagnetic materials, a contribution of the thermoelectric signal caused by spin-wave dynamics gives rise to thermally induced spurious signals [22–24]. Complementary to the dc voltage detection technique, a new method which is immune to the aforementioned spurious signals, the ac inductive method, was proposed by Berger *et al.* [25,26]. In this experimental approach, a static magnetic field is applied along the normal of a thin-film nonmagnetic/ferromagnetic bilayer and an ac magnetic field is applied using an adjacent microstrip line. An ac spin current is injected into the nonmagnetic material, which gets converted into an ac electric current via the spin to charge conversion. The generated ac

*Present address: Technische Universität Kaiserslautern, 67663 Kaiserslautern, Germany.

†mshiraishi@kuee.kyoto-u.ac.jp

TABLE I. Specifications of the silicon wafers regarding the ion implantation: dopant, acceleration voltage, and area dose. According to the targeted doping concentration, we adjusted the acceleration voltage and area dose based on the SRIM simulations.

No.	Dopant/targeted concentration [cm^{-3}]	Dose (10 keV) [cm^{-2}]	Dose (15 keV) [cm^{-2}]	Dose (30 keV) [cm^{-2}]
1	Phosphorus/ 1×10^{20}	1×10^{14}		5×10^{14}
2	Phosphorus/ 1×10^{19}	1×10^{13}		5×10^{13}
3	Phosphorus/ 1×10^{18}	1×10^{12}		5×10^{12}
4	Nondoped			
5	Boron/ 1×10^{18}	3×10^{12}	5×10^{12}	
6	Boron/ 1×10^{19}	3×10^{13}	5×10^{13}	
7	Boron/ 1×10^{20}	3×10^{14}	5×10^{14}	

current causes inductive voltages in the microstrip line, which result in perturbation of the transmission signal. By analyzing the transmission signal, the *spin-orbit torque conductivity* (σ^{SOT}) in, e.g., Pt/ $\text{Ni}_{80}\text{Fe}_{20}$ (Permalloy, Py) and Cu/Py bilayers can be calculated in a self-consistent way [26]. The spin-orbit torque conductivity quantifies the charge conversion efficiency starting from the precession dynamics of spins in the ferromagnet, including all the intermediating processes: spin current generation, spin current transmission through the interfaces, and spin to charge conversion.

We employed this method to investigate the spin to charge conversion physics in semiconductor-metal-ferromagnet hybrid devices. We thereby chose silicon, the vital material of modern electronics, and study the Si doping dependence of the spin-orbit torque conductivity of Si/Cu/Py trilayers.

II. EXPERIMENT

Dopant ions are implanted in commercially available Silicon-on-Insulator (SOI) wafers, which consist of a Si base layer (nominal resistivity is $1 \sim 2 \Omega\text{m}$) and a 200-nm-thick SiO_2 layer, and the top 100-nm-thick Si layer (nominal resistivity is $30 \sim 40 \Omega\text{m}$). The acceleration voltage was set to be 10 and 30 keV for phosphorus, and 10 and 15 keV for boron, respectively. Each dose was determined by SRIM (Stopping and Range of Ions in Matter) simulations beforehand to form a uniform doping profile along the depth direction. The detailed recipe of the ion implantation is presented in Table I. The doped wafers were treated in a rapid thermal annealing system for activation of the dopants. The measured resistivity of each implanted wafer is shown in Fig. 1. The heavier doping yielded the smaller resistivity in both phosphorus and boron doping. We cut the wafers into chips of $9 \times 8 \text{ mm}$ in size. After removing the natural oxidation layer by 10% hydrogen fluoride (HF) solution, a 3-nm-thick Cu interlayer and a 7-nm-thick Py layer were deposited by an electron-beam deposition system. The inserted Cu layer prevents the intermixing between Si and Py, enabling more qualified interface preparation. Cu is also known for being a good conductor of spin current, the spin-diffusion length of which is ca. 500 nm [27], which allows for a transparent spin current channel between Py and Si. The observed effective magnetization of the Py layer is comparable to that of intrinsic Py.

After fabrication of the samples, we followed the measurement procedure described in the literature [25]. As shown in Fig. 2, the ground signal ground (GSG)-type coplanar waveguide (CPW) was connected to the vector network an-

alyzer (VNA, N5225B, Keysight Technologies). The sample was placed on the CPW. A dc static magnetic field was applied perpendicular to the sample plane by an electromagnet. While the rf signal was transmitted from one port of the VNA to excite the FMR of the Py layer, the dc magnetic field was swept around the FMR resonance field of Py. The transmission signal S_{21} was measured at fixed frequency while stepping the dc magnetic field. These experiments were carried out for fixed frequencies from 10 to 30 GHz.

III. MODELING

The resonance field of the Py film follows the out-of-plane-type Kittel equation,

$$\frac{\omega}{\gamma} = \mu_0(H_{\text{res}} - M_{\text{eff}}). \quad (1)$$

Here, ω , γ , μ_0 , H_{res} , and M_{eff} are angular frequency, gyromagnetic ratio, vacuum permeability, resonance magnetic field, and effective magnetization, respectively. The aforementioned measurement scheme yields the complex transmission signal (S_{21}) as a function of the external dc magnetic field. Under the FMR condition of the Py layer, an ac spin current is injected into the adjacent nonmagnetic layers consisting of the Cu (3 nm) layer and the Si (100 nm) layer. When the ac spin current is converted to an ac charge current in the direction parallel to the CPW, the corresponding charge carriers give rise to an ac voltage response in the CPW. This can be understood as a change of the inductance of the

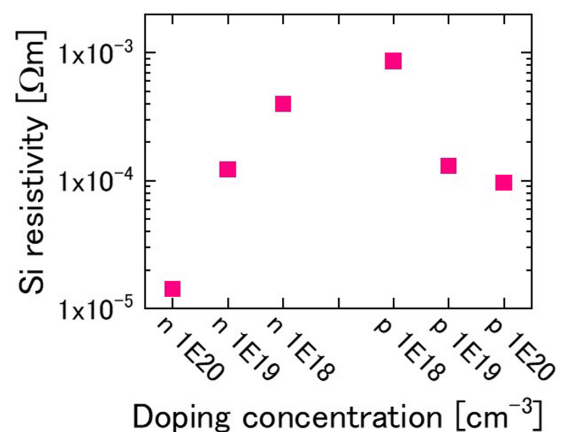


FIG. 1. Resistivity of the 100-nm-thick Si layers of the implanted SOI wafers probed by four-terminal resistance measurements.

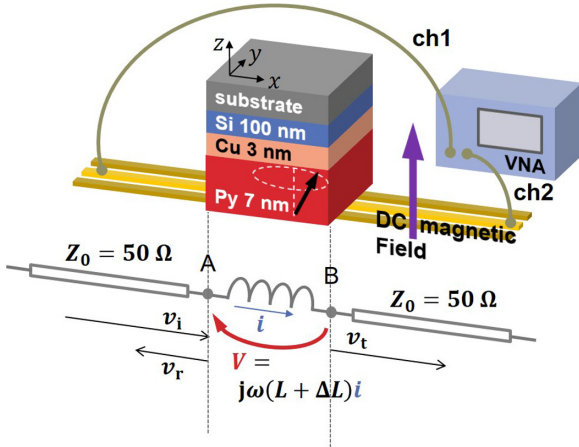


FIG. 2. Schematic illustration of the setup for the complex transmission measurement S_{21} . The CPW is connected with the two ports of the VNA using rf cables. The sample was placed on the CPW facing the Py. In addition, the figure shows the lumped element circuit model of the system, where the rf cables, the CPW, and the inductance lump of the sample are connected in series.

composite system of the CPW and the sample causing the modulation of S_{21} . By considering the continuity of voltage and current in a lumped element model of the whole system consisting of the serially connected rf cables, one can formulate an equation describing the inductive signal generation. Under the off-resonant condition, the continuity of the voltage between point A and point B in Fig. 2 gives

$$v_i + v_r - v_t = j\omega Li. \quad (2)$$

The continuity at the points A and B yields,

$$\frac{v_i}{Z_0} - \frac{v_r}{Z_0} = i, \quad (3a)$$

$$\frac{v_t}{Z_0} = i, \quad (3b)$$

respectively. Here, v_i , v_r , and v_t are entering, reflecting, and transmitting voltage amplitude (complex value). L and i are the off-resonant inductance and the current in the region between point A and point B. The characteristic impedance of the cables and the CPW is nominally 50Ω . After solving these equations, the transmission S_{21} is expressed as below,

$$S_{21} = \frac{v_t}{v_i} = \frac{2Z_0}{2Z_0 + j\omega L}. \quad (4)$$

When L changes to $L + \Delta L$ under the resonance condition, the perturbation of the transmission signal (ΔS_{21}) should be obtained by the partial derivative and its ratio to the baseline becomes a simple expression,

$$\frac{\Delta S_{21}}{S_{21}} = \frac{\partial S_{21}}{\partial L} \frac{\Delta L}{S_{21}} = \frac{-j\omega \Delta L}{2Z_0 + j\omega L} \approx \frac{-j\omega \Delta L}{2Z_0}. \quad (5)$$

Note that we neglected the relatively small contribution of $j\omega L$ in the denominator. One may be careful about the dissipation and phase-delay factors through the CPW and the two rf cables. These factors, however, are constant in off- and on-resonant states of the ferromagnet and eliminated by dividing by S_{21} . The change in the inductance ΔL is induced by (i) the ac dipolar magnetic field under the FMR, (ii) the spin to charge conversion current in odd phase, and (iii) the Fara-

day effect and the spin to charge conversion current in even phase with time reversal. In Fig. 1(d) in Ref. [25], the phase relation among the magnetic amplitude in the y direction (m_y), the odd and even current (j_o^{SOT} , j_e^{SOT}) via the spin to charge conversion, and the Faraday current (j_e^{F}) are shown. Note that j_o^{SOT} is at the phase quadrature to that of j_e^{SOT} and j_e^{F} , hence we can extract the inductance purely from j_o^{SOT} by decomposing an entire observed inductance into real and imaginary parts. The three components which contribute to the on-resonant inductance change have the same origin: precession of the magnetization. Therefore, ΔL is proportional to the polder's susceptibility tensor $\chi(\omega, H)$,

$$\Delta L = \tilde{L} \chi(\omega, H). \quad (6)$$

The complex value, \tilde{L} , is the normalized inductance, representing the dipolar contribution and the spin to charge conversion. The value of \tilde{L} can be determined by a curve fitting of the S_{21} spectra as a function of the magnetic field,

$$\frac{\Delta S_{21}}{S_{21}} \approx \frac{-j\omega \tilde{L} \chi(\omega, H)}{2Z_0}. \quad (7)$$

From the spectrum fitting using the measured values of $\frac{\Delta S_{21}}{S_{21}}(\omega, H)$, one can determine $\tilde{L}(\omega)$ and $\chi(\omega, H)$. The polder's susceptibility tensor $\chi(\omega, H)$ contains the resonance field and the linewidth of the spectra, from which the magnetic parameters of the Py layer were calculated. We emphasize that the measurement observable is a frequency- and magnetic field-dependent complex microwave transmission. As such only signals in the microwave domain are analyzed and hence make this technique immune to dc voltage signals, as observed in dc spin pumping and rectification experiments.

IV. RESULTS AND DISCUSSION

The g factor and the effective saturation magnetization, $\mu_0 M_{\text{eff}}$, of each sample determined by analyzing the resonance field and frequency of the FMR [Fig. 3(a)] are shown in Figs. 3(b) and 3(c), respectively. Whereas the deviations of g factor in all samples are within 0.5%, a notable decrease of $\mu_0 M_{\text{eff}}$ was observed for the highly doped samples, which suggests effects of the adjacent conductive layer on the saturation magnetization. The Gilbert damping constant, α , and the inhomogeneity broadening, $\mu_0 \Delta H_0$, were determined by the frequency dependence of the linewidth of the spectrum [Fig. 3(d)], where the measured linewidth equals $\mu_0 \Delta H_0 + 2\alpha\omega/\gamma$. As shown in Fig 3(e), the Gilbert damping constant does not show a discernible trend with doping, but it is scattered within 20% range. Only the highly doped p -type sample showed a relatively high $\mu_0 \Delta H_0$, as shown in Fig. 3(f). Though some of the magnetic parameters thus exhibit doping concentration dependence, the normalization by $\chi(\omega, H)$ in Eq. (7) accounts for the possible influence of the small modulation in the magnetic dynamics on $\tilde{L}(\omega)$.

Considering the geometry of the CPW, the sample and the spacing between these two components, \tilde{L} is expressed as [25]

$$\text{Re}(\tilde{L}) = \frac{\mu_0 l}{4} \left[\frac{d_{\text{FM}}}{W_{\text{wg}}} \eta^2 + \eta \frac{2L_{21}}{\mu_0 l M_s} \frac{\hbar \omega}{e} \sigma_{\text{Re}}^{\text{SOT}} \right], \quad (8a)$$

$$\text{Im}(\tilde{L}) = \frac{\mu_0 l}{4} \cdot \eta \frac{2L_{21}}{\mu_0 l M_s} \frac{\hbar \omega}{e} \sigma_{\text{Im}}^{\text{SOT}}. \quad (8b)$$

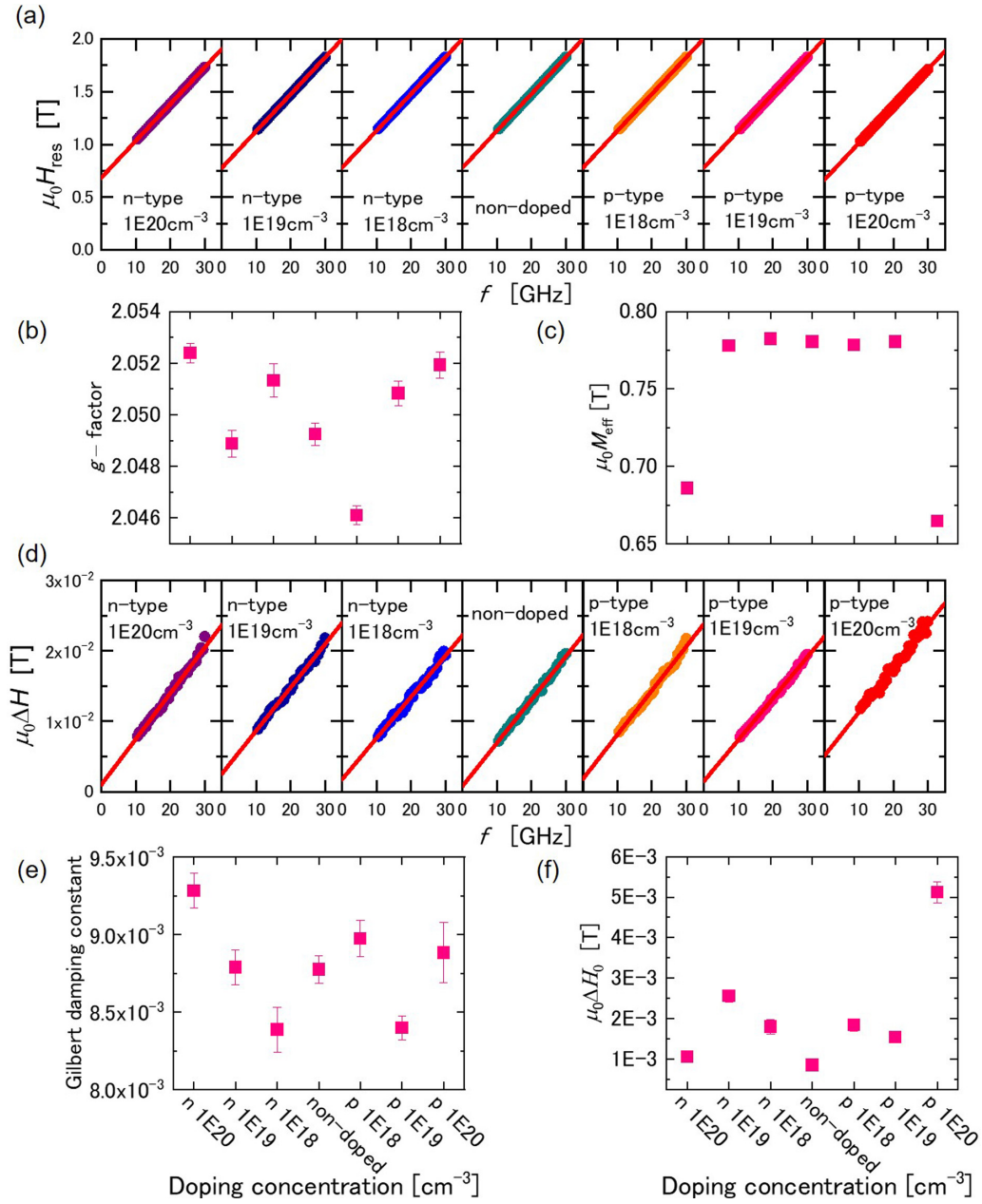


FIG. 3. Magnetic parameters were obtained by the VNA-FMR for each sample with different doping condition of the Si layer. The frequency dependence of the FRM resonance field is shown in (a) with the linear fittings, from which (b) g factor and (c) the effective magnetization $\mu_0 M_{\text{eff}}$ were determined. The frequency dependence of the linewidth is shown in (d) with the linear fittings, from which (e) Gilbert damping constant and (f) the inhomogeneity broadening of linewidth, $\mu_0 \Delta H_0$ were determined.

Here, μ_0 , \hbar , e , M_s are vacuum magnetic permeability, the Dirac constant, elementary charge, and the saturation magnetization of the ferromagnetic film. The geometrical factors: l , W_{wg} , d_{FM} , η , L_{21} , are the length of the sample, the width of the CPW signal line, the thickness of the ferromagnetic film, the spacing loss factor, and the mutual inductance between the CPW and the sample. The real and imaginary spin-orbit torque conductivity, $\sigma_{\text{Re}}^{\text{SOT}}$ and $\sigma_{\text{Im}}^{\text{SOT}}$, originate from the frequency-dependent current generation in the sample. Following Ref. [25], $\sigma_{\text{Re}}^{\text{SOT}}$ comes from the spin to charge conversion in the even phase and the Faraday current, and $\sigma_{\text{Im}}^{\text{SOT}}$ from the spin to charge conversion only in the odd phase. Thus, $\sigma_{\text{Im}}^{\text{SOT}}$ corresponds to the dampinglike conversion

from magnetization dynamics in the ferromagnetic metal to charge currents oscillating at the precession frequency. Both real and imaginary parts of \tilde{L} are linear functions of frequency. Therefore, we can determine $\sigma_{\text{Re}}^{\text{SOT}}$ and $\sigma_{\text{Im}}^{\text{SOT}}$ by linear fitting of \tilde{L} vs frequency.

In Figs. 4(a) and 4(b), the frequency dependence of the real and imaginary parts of the inductances \tilde{L} of each sample are shown. The phase-error correction [25] by imposing the prerequisite that \tilde{L} should be a real-valued number at the zero-frequency limit was already applied here. According to Eqs. (8), the coefficients of linear proportion consist of the geometrical parameters, the magnetic properties of the Py film, and more importantly, $\sigma_{\text{Re}}^{\text{SOT}}$ and $\sigma_{\text{Im}}^{\text{SOT}}$. Because the geometrical

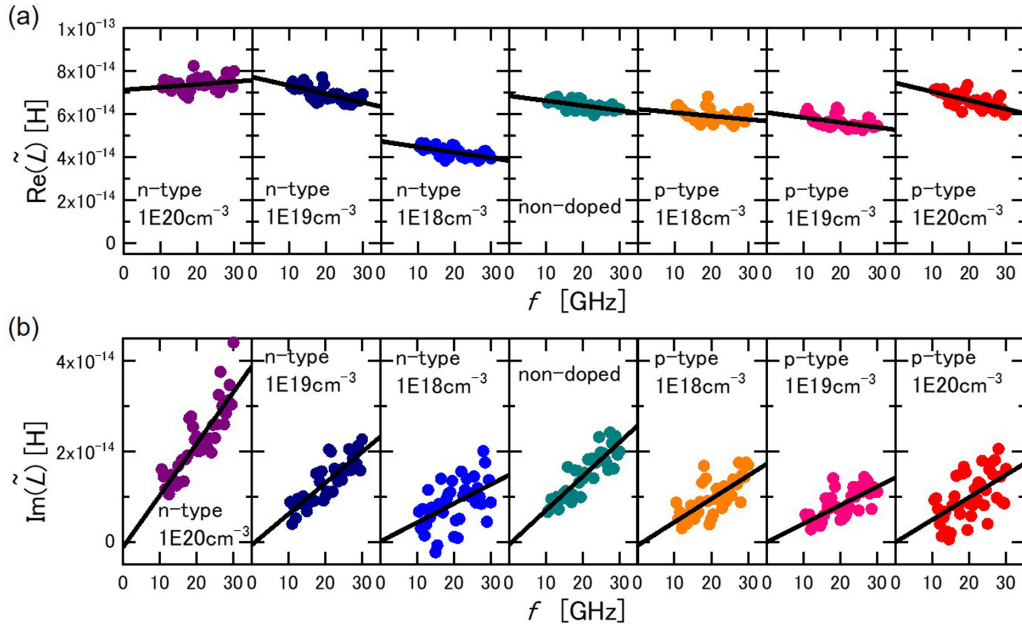


FIG. 4. (a) Real and (b) imaginary parts of the normalized inductances as a function of the rf frequency measured with the sample group of different doping conditions. The solid lines are linear fits. From the slopes of these fits, we can calculate the real and imaginary spin-orbit torque conductivities, $\sigma_{\text{Re}}^{\text{SOT}}$ and $\sigma_{\text{Im}}^{\text{SOT}}$.

parameters are in the same range in the measured samples, a rough estimation of $\sigma_{\text{Re}}^{\text{SOT}}$ and $\sigma_{\text{Im}}^{\text{SOT}}$ is given by the steepness of the linear slopes of $\text{Re}(\tilde{L})$ and $\text{Im}(\tilde{L})$.

To determine the exact value of $\sigma_{\text{Re}}^{\text{SOT}}$ and $\sigma_{\text{Im}}^{\text{SOT}}$, a comprehensive linear fitting was conducted for $\text{Re}(\tilde{L})$ and $\text{Im}(\tilde{L})$ by using the geometrical parameters and the effective saturation magnetization, M_{eff} , obtained from the FMR resonance field, as a saturation magnetization, M_s , appearing in Eqs. (8). We note that the spacing d between the CPW and the sample changes in each measurement, altering $\eta(l, d)$ and $L_{21}(l, d)$ defined in Ref. [25], but d is analytically determined by the zero-frequency limit of $\text{Re}(\tilde{L})$, which represents the dipolar contribution from the magnetic precession of the Py film. We repeated the determination process of $\sigma_{\text{Re}}^{\text{SOT}}$ and $\sigma_{\text{Im}}^{\text{SOT}}$ for the seven samples, with results shown in Figs. 5(a) and 5(b).

We first focus on the results for the reference sample with nondoped Si. Here, we find $\sigma_{\text{Im}}^{\text{SOT}}$ of comparable magnitude to that reported in Ref. [26] for a Py/Cu(4.5-nm) bilayer. The $\sigma_{\text{Im}}^{\text{SOT}}$ for the reference sample may originate from (i) the inverse spin Hall effect (ISHE) in the Cu interlayer and (ii) the self-induced ISHE [28] in the Py layer due to a possible imbalance of spin absorption at the top and the bottom surface, and (iii) sizable spin-orbit torques in a ferromagnet itself [29–37]. We assume that this spin charge conversion effect is present in all our samples. To discuss the influence of doping on spin charge conversion in our Si/Cu/Py trilayers, we then calculate $\Delta\sigma_{\text{Re/Im}}^{\text{SOT}} = \sigma_{\text{Re/Im}}^{\text{SOT}} - \sigma_{\text{Re/Im}}^{\text{SOT}}(\text{nondoped Si})$ shown in Figs. 5(c) and 5(d). The observed $\Delta\sigma_{\text{Re/Im}}^{\text{SOT}}$ are also on the order of $10^4 \Omega^{-1} \text{ m}^{-1}$ (e. g., $\Delta\sigma_{\text{Im}}^{\text{SOT}}$ in the most heavily doped p -type sample), which is in the same magnitude range as Py/Cu systems [25]. Using the Pt-based systems, where enhanced spin to charge conversion efficiency is expected,

previous studies observed a significantly larger spin-orbit torque conductivity [25,26].

We focus on $\Delta\sigma_{\text{Im}}^{\text{SOT}}$ originating from the spin to charge conversion in the odd phase, i.e., with symmetry of the ISHE. The calculated $\Delta\sigma_{\text{Im}}^{\text{SOT}}$ for each measured sample is shown in Fig. 5(d). A decreasing trend of $\Delta\sigma_{\text{Im}}^{\text{SOT}}$ with the transition from n -type to p -type doping was observed. We note that $\Delta\sigma_{\text{Im}}^{\text{SOT}}$ with the opposite sign relative to that in the nondoped samples was observed in the n -type and p -type samples. The minimum change of $\Delta\sigma_{\text{Im}}^{\text{SOT}}$ between them is $1.4 \times 10^4 \Omega^{-1} \text{ m}^{-1}$, considering the fit errors. The doping concentration for these two samples, $1 \times 10^{20} \text{ cm}^{-3}$, exceeds the effective densities of states of Si in the conduction band ($2.8 \times 10^{19} \text{ cm}^{-3}$) and valence band ($2.65 \times 10^{19} \text{ cm}^{-3}$) [38]. In these doping levels, no depletion layer between Si and Cu is formed at the Si/Cu interfaces in the n -type and p -type samples allowing carriers to transverse through the interface. In this situation [Fig. 6(a) for n type and Fig. 6(b) for p type], the spin current in the Cu layer can travel through the interface between the Cu layer and the degenerate Si. In this case, a possible ISHE in Si can contribute to spin charge conversion. In the spin-scattering process associated with the ISHE, the directions of the scattered charge are governed by its spin polarization irrespective of its charge. Therefore, when the carrier of the Si layer is switched by change of dopant, the sign of θ_{SH} is also switched. This mechanism can explain the measured $\sigma_{\text{Im}}^{\text{SOT}}$ in the n -type and p -type samples with the doping concentration of $1 \times 10^{20} \text{ cm}^{-3}$. Next, we focus on the nondegenerate Si samples. Considering the work function of Cu (4.5 eV) [39] and the electron affinity (4.05 eV) [38] of Si, the ideal band alignment model teaches us the barrier height is 0.45 eV. Furthermore, experimental studies reported that the

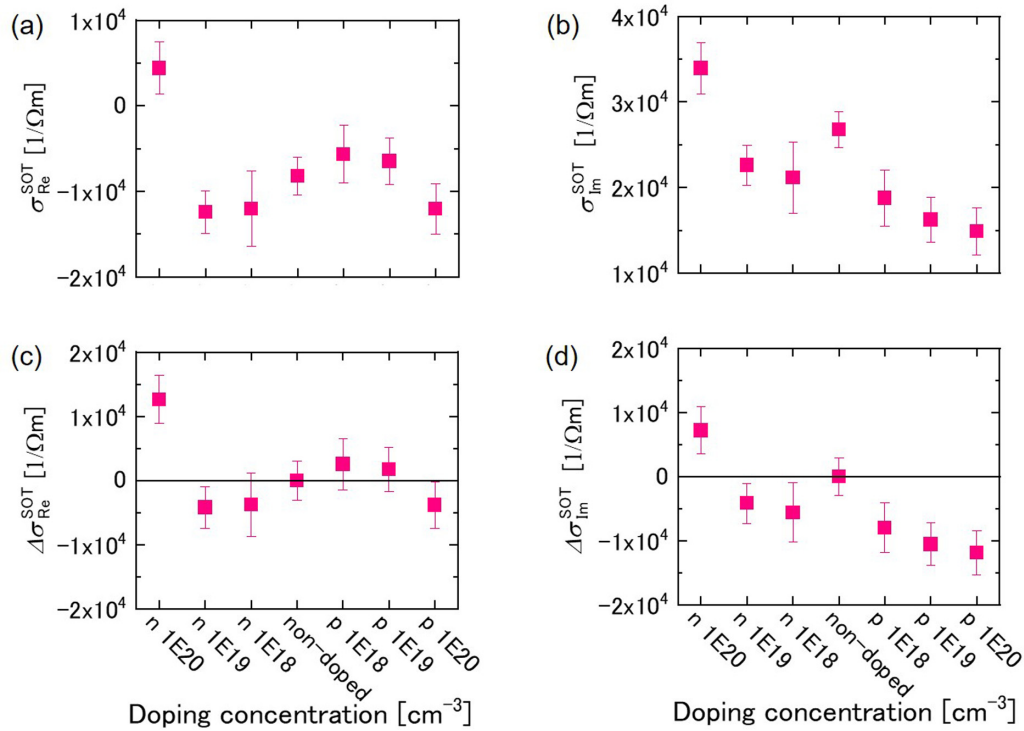


FIG. 5. (a) Real spin-orbit torque conductivity ($\sigma_{\text{Re}}^{\text{SOT}}$) of the measured samples. (b) Imaginary spin-orbit torque conductivity ($\sigma_{\text{Im}}^{\text{SOT}}$) of the measured samples. (c) Change of real spin-orbit torque conductivity ($\sigma_{\text{Re}}^{\text{SOT}}$) from that of the nondoped sample. (d) Change of imaginary spin-orbit torque conductivity ($\sigma_{\text{Im}}^{\text{SOT}}$) from that of the nondoped sample. Beneath the x axis, the dopant type and doping concentration of each sample are described.

Fermi level located around the middle of the band gap of Si in a Cu/Si system [40]. Hence, a schematic viewgraph at the interface can be described as shown in Fig. 6(c) for n -type Si and Fig. 6(d) for p -type Si. Existence of the depletion layer

hinders the Ohmic conduction of spin current through the Cu/Si interface, resulting in the decrease of the spin-mixing conductance, $G_{\uparrow\downarrow}$ accompanied by a decrease of $\Delta\sigma_{\text{Im}}^{\text{SOT}}$. In Fig. 5, magnitudes of the $\Delta\sigma_{\text{Im}}^{\text{SOT}}$ of the nondegenerate Si samples (n - and p -type, 10^{18} and 10^{19} cm^{-3}) are smaller than those of the degenerate samples, indicating insufficient ISHE current generation in the Si layer due to the decreased $G_{\uparrow\downarrow}$. We note that a slight but clear shift of $\Delta\sigma_{\text{Im}}^{\text{SOT}}$ from the baseline of nondoped Si can be seen with the p -type nondegenerate samples, which is attributed to the fact that the SOI in p -Si is stronger than that in n -Si at the same doping concentration as suggested by its band structures.

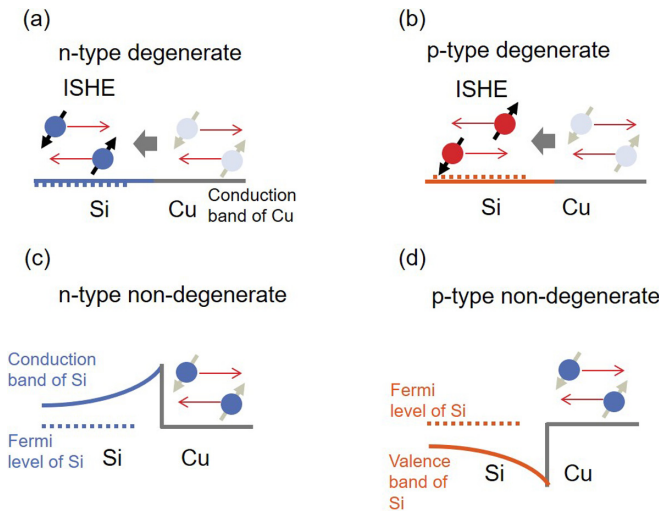


FIG. 6. Spatial band diagrams of the interfaces between (a) n -type degenerate Si/Cu, (b) p -type degenerate Si/Cu, (c) n -type nondegenerate Si/Cu, (d) p -type nondegenerate Si/Cu. The Fermi level of Si is indicated with dashed lines and the conduction/valence band of Si is indicated with solid lines. In the degenerate cases, carriers can flow into the Si side, where the ISHE takes place. In the nondegenerate case, carriers are partially blocked at the interface.

Finally, we comment on doping dependence of $\sigma_{\text{Re}}^{\text{SOT}}$ shown in Fig. 5(a). According to Ref. [25], $\sigma_{\text{Re}}^{\text{SOT}}$ equals $\sigma_{\text{e}}^{\text{F}} - \sigma_{\text{e}}^{\text{SOT}}$, where $\sigma_{\text{e}}^{\text{F}}$ is the Faraday conductivity and $\sigma_{\text{e}}^{\text{SOT}}$ is the spin-orbit torque conductivity, both of which appear in the even phase expected for spin to charge conversion by the inverse Rashba-Edelstein effect (IREE). Because the Faraday current density depends on the total conductivity of the sample, irrespective of the carrier type, $\sigma_{\text{e}}^{\text{F}}$ should be constant considering the conductance difference of the stack of the 7-nm-thick Py layer and the 3-nm-thick Cu layer to the 100-nm Si layer. Therefore, the deviations from the baseline of the $\Delta\sigma_{\text{Re}}^{\text{SOT}}$ for the nondoped sample are tentatively attributed to $\sigma_{\text{e}}^{\text{SOT}}$ by the IREE. In Fig. 5(c), nonzero $\Delta\sigma_{\text{e}}^{\text{SOT}}$ within fit error is only observed for the degenerate n -doped sample and could be caused by a Rashba electric field at the Cu/Si interface. For the nondegenerate samples and the degenerate p -doped sample, no significant change of $\sigma_{\text{e}}^{\text{SOT}}$ is observed with doping. It is most likely that the Rashba electric field intensity is not

sufficiently strong in the Cu/Si interface for these samples to induce observable σ_e^{SOT} by the IREE.

V. CONCLUSION

In this study, we conducted inductive ac measurements of Si/Cu/Py trilayer samples with different doping concentrations in Si. The obtained results indicated successful modulation of the spin-orbit torque conductivity of the Si/Cu/Py systems by controlling the Si carrier type and doping concentration. A doping dependence of $\sigma_{\text{Im}}^{\text{SOT}}$, compatible with the ISHE in the Si, was observed in the transition from n -type to p -type doping. In the degenerate Si samples, the relative sign of $\sigma_{\text{Im}}^{\text{SOT}}$ changed between n -type and p -type doping. Our results are in qualitative agreement with the doping dependence of the formation of the depletion layer and its thickness, and by the impurity scattering rate of carriers. This systematic study of σ_0^{SOT} of Si/Cu/Py systems with various doping concentrations provides insight towards exploration for spin

current physics of semiconductors and demonstrates the application of a technique to experimentally determine spin to charge conversion in ferromagnet/semiconductor hybrids.

ACKNOWLEDGMENTS

E.S. acknowledges the JSPS Research Fellowship for Young Researchers. E.S. also acknowledges travel support of Mazume Award (Dept. of Eng., Kyoto University). L.L. and M.W. acknowledge financial support by the German research foundation (DFG) via Project No. WE 5386/4-1, H.H. acknowledges financial support from the Deutsche Forschungsgemeinschaft via Germany's Excellence Strategy No. EXC-2111-390814868. This work is partially supported by a Grant-in-Aid for Scientific Research (S) No. 16H06330, a Grant-in-Aid for Young Scientists (A) No. 16H06089, JSPS KAKENHI Grant No. 17J09520, and Grant-in-Aid for Research Activity Start-up No. 20K22413. The ion implantation and the rapid thermal annealing was implemented with the support of Nano-technology Platform at Nagoya University.

-
- [1] J. E. Hirsch, *Phys. Rev. Lett.* **83**, 1834 (1999).
 [2] E. Saitoh, M. Ueda, H. Miyajima, and G. Tatara, *Appl. Phys. Lett.* **88**, 182509 (2006).
 [3] P. R. Hammar, B. R. Bennett, M. J. Yang, and M. Johnson, *Phys. Rev. Lett.* **83**, 203 (1999).
 [4] H. L. Wang, C. H. Du, Y. Pu, R. Adur, P. C. Hammel, and F. Y. Yang, *Phys. Rev. B* **88**, 100406(R) (2013).
 [5] K. Ando and E. Saitoh, *Nat. Commun.* **3**, 629 (2012).
 [6] K. Ando, S. Takahashi, J. Ieda, H. Kurebayashi, T. Trypiniotis, C. H. W. Barnes, S. Maekawa, and E. Saitoh, *Nat. Mater.* **10**, 655 (2011).
 [7] H. L. Wang, C. H. Du, Y. Pu, R. Adur, P. C. Hammel, and F. Y. Yang, *Phys. Rev. Lett.* **112**, 197201 (2014).
 [8] C. Du, H. Wang, F. Yang, and P. C. Hammel, *Phys. Rev. B* **90**, 140407(R) (2014).
 [9] D. Tian, Y. Li, D. Qu, S. Y. Huang, X. Jin, and C. L. Chien, *Phys. Rev. B* **94**, 020403(R) (2016).
 [10] K. S. Das, W. Y. Schoemaker, B. J. van Wees, and I. J. Vera-Marun, *Phys. Rev. B* **96**, 220408(R) (2017).
 [11] T. Wimmer, B. Coester, S. Geprägs, R. Gross, S. T. B. Goennenwein, H. Huebl, and M. Althammer, *Appl. Phys. Lett.* **115**, 092404 (2019).
 [12] Y. Tserkovnyak, A. Brataas, and G. E. W. Bauer, *Phys. Rev. Lett.* **88**, 117601 (2002).
 [13] O. Mosendz, J. E. Pearson, F. Y. Fradin, G. E. W. Bauer, S. D. Bader, and A. Hoffmann, *Phys. Rev. Lett.* **104**, 046601 (2010).
 [14] F. D. Czeschka, L. Dreher, M. S. Brandt, M. Weiler, M. Althammer, I.-M. Imort, G. Reiss, A. Thomas, W. Schoch, W. Limmer, H. Huebl, R. Gross, and S. T. B. Goennenwein, *Phys. Rev. Lett.* **107**, 046601 (2011).
 [15] D. Hou, Z. Qiu, K. Harii, Y. Kajiwara, K. Uchida, Y. Fujikawa, H. Nakayama, T. Yoshino, T. An, K. Ando, X. Jin, and E. Saitoh, *Appl. Phys. Lett.* **101**, 042403 (2012).
 [16] H. Emoto, Y. Ando, G. Eguchi, R. Ohshima, E. Shikoh, Y. Fuseya, T. Shinjo, and M. Shiraishi, *Phys. Rev. B* **93**, 174428 (2016).
 [17] Y. Shiomi, K. Nomura, Y. Kajiwara, K. Eto, M. Novak, K. Segawa, Y. Ando, and E. Saitoh, *Phys. Rev. Lett.* **113**, 196601 (2014).
 [18] H. J. Juretschke, *J. Appl. Phys.* **31**, 1401 (1960).
 [19] W. G. Egan and H. J. Juretschke, *J. Appl. Phys.* **34**, 1477 (1963).
 [20] Y. S. Gui, N. Mecking, X. Zhou, G. Williams, and C.-M. Hu, *Phys. Rev. Lett.* **98**, 107602 (2007).
 [21] A. Brataas, Y. Tserkovnyak, G. E. W. Bauer, and B. I. Halperin, *Phys. Rev. B* **66**, 060404(R) (2002).
 [22] P. Wang, L. F. Zhou, S. W. Jiang, Z. Z. Luan, D. J. Shu, H. F. Ding, and D. Wu, *Phys. Rev. Lett.* **120**, 047201 (2018).
 [23] O. Wid, J. Bauer, A. Müller, O. Breitenstein, S. S. P. Parkin, and G. Schmidt, *Sci. Rep.* **6**, 28233 (2016).
 [24] E. Shigematsu, Y. Ando, S. Dushenko, T. Shinjo, and M. Shiraishi, *Appl. Phys. Lett.* **112**, 212401 (2018).
 [25] A. J. Berger, E. R. J. Edwards, H. T. Nembach, A. D. Karenowska, M. Weiler, and T. J. Silva, *Phys. Rev. B* **97**, 094407 (2018).
 [26] A. J. Berger, E. R. J. Edwards, H. T. Nembach, O. Karis, M. Weiler, and T. J. Silva, *Phys. Rev. B* **98**, 024402 (2018).
 [27] T. Kimura, J. Hamrle, and Y. Otani, *Phys. Rev. B* **72**, 014461 (2005).
 [28] A. Tsukahara, Y. Ando, Y. Kitamura, H. Emoto, E. Shikoh, M. P. Delmo, T. Shinjo, and M. Shiraishi, *Phys. Rev. B* **89**, 235317 (2014).
 [29] K.-W. Kim, K.-J. Lee, J. Sinova, H.-W. Lee, and M. D. Stiles, *Phys. Rev. B* **96**, 104438 (2017).
 [30] Y. Kageyama, Y. Tazaki, H. An, T. Harumoto, T. Gao, J. Shi, and K. Ando, *Sci. Adv.* **5**, eaax4278 (2019).
 [31] W. Wang, T. Wang, V. P. Amin, Y. Wang, A. Radhakrishnan, A. Davidson, S. R. Allen, T. J. Silva, H. Ohldag, D. Balzar, B. L. Zink, P. M. Haney, J. Q. Xiao, D. G. Cahill, V. O. Lorenz, and X. Fan, *Nat. Nanotechnol.* **14**, 819 (2019).
 [32] M. Haidar, A. A. Awad, M. Dvornik, R. Khymyn, A. Houshang, and J. Åkerman, *Nat. Commun.* **10**, 2362 (2019).

- [33] L. Liu, J. Yu, R. González-Hernández, C. Li, J. Deng, W. Lin, C. Zhou, T. Zhou, J. Zhou, H. Wang, R. Guo, H. Y. Yoong, G. M. Chow, X. Han, B. Dupé, J. Železný, J. Sinova, and J. Chen, *Phys. Rev. B* **101**, 220402(R) (2020).
- [34] M. Tang, K. Shen, S. Xu, H. Yang, S. Hu, L. Weiming, C. Li, M. Li, Z. Yuan, S. J. Pennycook, K. Xia, A. Manchon, S. Zhou, and X. Qiu, *Adv. Mater.* **32**, 2002607 (2020).
- [35] R. Q. Zhang, L. Y. Liao, X. Z. Chen, T. Xu, L. Cai, M. H. Guo, H. Bai, L. Sun, F. H. Xue, J. Su, X. Wang, C. H. Wan, H. Bai, Y. X. Song, R. Y. Chen, N. Chen, W. J. Jiang, X. F. Kou, J. W. Cai, H. Q. Wu, F. Pan, and C. Song, *Phys. Rev. B* **101**, 214418 (2020).
- [36] J. W. Lee, J. Y. Park, J. M. Yuk, and B.-G. Park, *Phys. Rev. Appl.* **13**, 044030 (2020).
- [37] D. Céspedes-Berrocal, H. Damas, S. Petit-Watelot, D. Maccariello, P. Tang, A. Arriola-Córdova, P. Vallobra, Y. Xu, J.-L. Bello, E. Martin, S. Migot, J. Ghanbaja, S. Zhang, M. Hehn, S. Mangin, C. Panagopoulos, V. Cros, A. Fert, and J.-C. Rojas-Sánchez, [arXiv:2010.09137](https://arxiv.org/abs/2010.09137).
- [38] S. M. Sze and K. K. Ng, *Physics of Semiconductor Devices*, 3rd ed. (John Wiley & Sons, Hoboken, NJ, 2007).
- [39] M. Grundmann, *The Physics of Semiconductors*, 2nd ed. (Springer-Verlag, Berlin, 2010).
- [40] M. O. Aboelfotoh, A. Cros, B. G. Svensson, and K. N. Tu, *Phys. Rev. B* **41**, 9819 (1990).